1
2
3   REVISION 1
4
5   TITLE: Electronic structure effects in the vectorial bond-valence model
6
7   REVISION 1
8
9

10   Barry R. Bickmore[1], Matthew F. C. Wander[2], Joel Edwards[1,*], Josh Maurer[1], Kendrick
11   Shepherd[3], Eric Meyer[1], W. Joel Johansen[1], Rose A. Frank[1], Charles Andros[1], and
12   Matthew Davis[1]
13
14   [1] Department of Geological Sciences, Brigham Young University, Provo, UT 84602,
15   U.S.A. E-mail: barry_bickmore@byu.edu
16
17   [2] Department of Chemistry and Biochemistry, Baylor University, Waco, TX 76701,
18   U.S.A.
19
20   [3] Department of Civil Engineering, Brigham Young University, Provo, UT 84602,
21   U.S.A.
22
23
24
25
26   [*] Present address: Nevada Bureau of Mines and Geology, University of Nevada, MS
27   178, Reno, NV 89557, U.S.A.

28   Abstract

29   The vectorial bond-valence model (VBVM) describes the spatial distribution of

30 bonds to each atom in a system in terms of the vector sum of the incident bond valences.

31 It has been applied in the past to cations not subject to electronic structure effects (e.g.,

32 lone-pair or Jahn-Teller effects,) in which case the expectation is that the vector sum will

33 be approximately zero. Here we analyze 178 simple-oxide crystal structures and show

34 that the vectorial bond-valence sum is a predictable function of the atomic valence

35 (oxidation state) of each atom and the valence of the strongest bond to atoms for which

36 second-order Jahn-Teller and lone-pair effects play a role in determining molecular

37 geometry. Outliers are uniformly metastable or unstable under ambient conditions,

38 suggesting that deviation from ideal vectorial bond-valence sums might be used as a

39 proxy for some aspect of structural potential energy. These results are all strictly in

40 harmony with the VSEPR model of molecular geometry, but may allow for more

41 quantitative prediction.

42

43 **Keyword**: crystal structure, oxide, bond valence, vectorial bond-valence model,

44 electronegativity, lone pair, second-order Jahn-Teller effect, spherical symmetry,

45 minimum coordination number

46

47

48   Introduction

49   The bond-valence model (BVM) has become a standard in inorganic chemistry

50   for predicting acceptable combinations of bonds, with their corresponding lengths, to ions

51   in solid structures, as well as for assessing unknown oxidation states of ions in crystals

52   (Brown, 2002; 2009). It is now commonplace (e.g., Müller et al., 2003) to assess the

53   plausibility of proposed crystal structures in terms of their adherence to the valence-sum

54   rule, which states that in a stable crystal structure, the valence of bonds incident to an ion

55   should ideally counterbalance the atomic valence of the ion. (See the *Theory* section

56   below for details.) Bickmore et al. (2009) recently used *ab initio* molecular dynamics

57   simulations to show that the valence-sum rule applies on a time-averaged basis to liquid

58   structures, in addition to solids.

59   Simple structural models like the BVM, e.g., the Lewis model and the valence

60   shell electron pair repulsion (VSEPR) model, have historically been very important for

61   generating new ideas about, for example, reaction mechanisms (Brown, 2003). And yet,

62   the BVM stands apart from the others because of its ability to make quantitative

63   predictions of bond lengths via the valence-sum rule. The BVM is conceptually and

64   mathematically very simple, as it boils down complex, multi-body interactions into a

65   single parameter, the bond-valence sum, which is predictive for many systems.

66   Even in cases where known structures deviate significantly from BVM

67   predictions, the model can prove useful by identifying which aspects of the molecular

68   structure cause the strain. If the valence-sum rule puts constraints on structures, it

69   follows that deviation from the rule entails some energetic cost. A number of

70   quantitative structure-activity relationships (QSARs) have been formulated based

71   partially on energy cost functions for deviation from the valence-sum rule (Salinas-

72   Sanchez et al., 1992; Hiemstra et al., 1996; Adams, 2001; Adams and Swenson, 2002;

73   Adams et al., 2004; Bickmore et al., 2004; Bickmore et al., 2006; Adams and Rao, 2009;

74   Perez-Mato et al., 2009). In fact, Rappe and coworkers have constructed a molecular

75   mechanics force field based on such a cost function, along with a number of more

76   standard potential energy terms (Grinberg et al., 2002; Cooper et al., 2003; Grinberg et

77   al., 2004; Shin et al., 2005).

78   BVM-based energy cost functions are attractive because bond-valence

79   calculations are empirically calibrated for different cation-anion pairs, so that the end

80   product (bond valence) is a common currency, no matter what types of atoms are

81   involved. This point is well illustrated by the work of Angel and colleagues, who showed

82   that the rate of change of bond-valence sums with pressure is constant for cations in both

83   the A and B sites in ABO_3 perovskites (Zhao et al., 2004a; b; Angel et al., 2005b; Angel

84   et al., 2005a; Zhao et al., 2006). Such a relationship would be very unlikely if the bond

85   valence-energy relationship were substantially different for A-O and B-O bonds.

86   QSARs based solely on the valence-sum rule necessarily have limited

87   applicability, because they are an incomplete description of molecular structure. Since

88   bond valences are only calculated between cations and anions, the model obviously

89   neglects non-bonded forces such as would be needed to describe ligand-ligand

90   interactions. And even if non-bonded interactions were addressed in the BVM, the

91   valence-sum rule is non-directional, i.e., concerned with the lengths of bonds between

92   cations and anions, but not with the spatial distribution of those bonds, so the BVM could

93   not deal with electronic structure effects. In cases where these other factors are

94   important, the BVM cannot fully address how molecular structure affects stability and

95   reactivity.

96   To maximize the quantitative usefulness of the BVM, it would be worthwhile to

97   expand the model to predict more aspects of condensed-phase structures. Harvey et al.

98   (2006) partially addressed this problem by proposing the vectorial bond-valence model

99   (VBVM), which incorporates some predictions of the Valence Shell Electron Pair

100   Repulsion (VSEPR) model (Gillespie and Hargittai, 1991) within a bond-valence

101   framework. VSEPR has been very successful at predicting bond angles and basic

102   molecular shapes, but does not quantitatively address bond lengths. In the VBVM, the

103   bonds incident to an atom are treated as vectors in the direction from the center of a

104   cation to the center of a coordinating anion, with magnitude equal to the bond valence.

105   Harvey et al. (2006) postulated that the sum of the valence vectors about a cation should

106   ideally be around zero, and showed that this postulate works well for group 12 cations

107   coordinated by 2-3 organic ligands, even when those ligands are multi-dentate. Lufaso

108   and Woodward (2001) used this postulate to accurately predict the positions of cations in

109   perovskite structures. Thus, the vector sum postulate reproduces the VSEPR prediction

110   that ligands will generally distribute themselves as symmetrically as possible about a

111   central atom. Harvey et al. (2006) acknowledged, however, that their vector sum

112   postulate is incomplete because it does not account for the influence of electronic

113   structure effects such as those due to lone pairs, which is one of the great successes of

114   VSEPR.

115   In this contribution, we explore a number of oxide structures to show how, by

116   using a novel definition of coordination number, the VBVM can be generalized to

117   address certain types of electronic structure effects. We also show how ideal vectorial

118   bond-valence sums can be estimated solely upon the basis of electron configuration and

119   coordination environment, and provide a preliminary evaluation of the potential for using

120   deviation from these ideal values as a proxy for some aspect of structural potential

121   energy.

122   Theory

123   Bond Valence

124   The concept of bond valence stems from Pauling's (1929) treatment of oxidation

125   number, or atomic valence (V), as a measure of an ion's bonding power, which is

126   distributed among any bonds incident to it. More recently, Preiser et al. (1999) showed

127   that the valence of individual bonds can be rationalized in terms of the electric flux

128   between charged centers, and Gibbs et al. (2003; 2004) showed that bond valence

129   correlates well with electron density at bond-critical points.

130   Bond valence is typically estimated via Eqn. 1 (e.g., Brown and Altermatt, 1985):

131

132                           $$s_{ij} = e^{\left((R_0 - R)/B\right)}$$ (1)

133

134   where s_{ij} is bond valence in valence units (v.u.) between ions i and j, R is bond length, R_0

135   is the bond length at which $s_{ij} = 1$ v.u., and B is another length term that describes the

136   softness of the bond type. Both R_0 and B are empirical valence parameters specific to a

137   given cation-anion pair, averaged over many structures.

138   The relative energetic favorability of a particular coordination environment for

139   ion i can be assessed by calculating the valence sum (S_i):

140

$$S_i = \sum_j s_{ij} \tag{2}$$

142

143   where the valence of each bond is positive in the direction of the anion and negative in

144   the direction of the cation. This simple treatment of the relationship between bond

145   valence and bond length usually results in bond-valence sums incident to both cations

146   and anions that are very close to the ideal, which is described by the valence-sum rule

147   (Brown and Altermatt, 1985; Brown, 2002).

148

$$S_i + V_i = 0 \tag{3}$$

150

151   That is, in a stable structure, the summed valence of bonds incident to an ion (S_i) ideally

152   should exactly counterbalance its atomic valence (V_i).

153   VSEPR and VBVM

154   The VSEPR model explains the spatial distribution of bonds about a central atom

155   via repulsion between electron pairs in the valence shell, including both lone pairs and

156   bonded pairs. To determine an ideal molecular geometry, one first finds the number of

157   valence-shell electron pairs, and then considers how the pairs can be arranged on a sphere

158   around the atom to achieve minimum energy due to repulsion between the pairs

159   (Gillespie and Hargittai, 1991). E.g., the O^{2-} in an H_2O molecule has two bonded

160   electron pairs with H and two lone pairs, and so ideally the electron pairs would be

161   distributed in a tetrahedron about the O^{2-}, giving rise to $\angle HOH = 109.5°$. This is fairly

162   close to the actual bond angle for a water molecule, $\angle HOH = 104.5°$.

163   Ideal molecular shapes, then, can be rationalized in terms the valence-bond

164   formulas of the atoms involved, but deviations from ideal geometries are due to a number

165   of factors (Müller, 2007).   1) Bonded pairs repel others less than lone pairs. Hence

166    $\angle HOH$ in water is smaller than the ideal tetrahedral angle. 2) Multiple bonds (e.g.,

167   double or triple bonds) repel other electron pairs to a greater degree than single bonds. 3)

168   The size of the ligands (i.e., the degree of repulsion among ligands) can also affect the

169   degree of distortion. Finally, 4) the electronegativity of the ligands, relative to the central

170   atom, determines the distribution of electron density along bond axes, and thus how

171   effectively bonded pairs repel other electron pairs around the central atom.

172   In the VBVM, bonds are treated as vectors in the direction from the cation center

173   to the anion center, with magnitude equal to the bond valence ($\vec{\mathbf{s}}_{ij}$). Brown (1988) and

174   Harvey et al. (2006) showed that the sum of the bond-valence vectors around a central

175   cation ($\vec{\mathbf{S}}_i$) very often has a magnitude close to 0 v.u. Harvey et al. (2006) formalized this

176   principle, which they called the "Valence Vector Sum Postulate":

177

178
$$\vec{\mathbf{S}}_i = \sum_j \vec{\mathbf{s}}_{ij} \approx \vec{0} \tag{4}$$

179

180   When the norm of the vector sum ($\lVert \vec{\mathbf{S}}_i \rVert$) deviates from 0, it is a good single-parameter

181   descriptor of the degree to which factors such as steric and electronic structure effects

182   (e.g., lone pairs) have distorted the bonding geometry (Brown, 1988).

183   The valence vector sum postulate (Eqn. 4) can reproduce some VSEPR

184   predictions. For example, cations with no lone pairs should ideally adopt a spherically

185   symmetrical coordination sphere, and stronger bonds tend to repel weaker ones since this

186   behavior would tend to minimize $\|\vec{\mathbf{S}}_i\|$. However, ligand-ligand interaction, as well as

187   the spatial distribution of bonds as a function of ligand electronegativity, coordination

188   number, and the presence of electronic distortions, has so far not been addressed.

189   Coordination number (N_c) and electronegativity (E_n)

190   While we do not address ligand-ligand interactions here, it may be that we can

191   largely predict the effect of some types of electronic distortions on $\|\vec{\mathbf{S}}_i\|$ by taking into

192   account the effects of N_c and E_n. If this is our goal, however, standard definitions of N_c

193   and E_n are problematic.

194   When determining N_c, some cutoff distance is typically defined and all

195   neighboring atoms within that distance are counted equally, while those outside are not

196   counted at all. The cutoff distance is usually short enough to exclude weaker interactions

197   that nevertheless exert a discernible influence, but long enough so interactions of very

198   different strengths are all counted equally. This makes N_c a discontinuous function of the

199   atomic environment, where small changes would sometimes cause large jumps in N_c,

200   while relatively large changes would sometimes cause no change in N_c.

201   Such a blunt instrument would necessarily lead to poor correlations with a

202   quantity like $\|\vec{\mathbf{S}}_i\|$, which can take into account subtle differences in bond strength.

203   Clearly, we require a more subtle definition of coordination number, like the following:

204

205                $$N_{min,i} = \left.|V_i|\middle/ s_{max,i}\right.$$ (6)

206

207

208   where $N_{min,i}$ is the minimum coordination number, which is the absolute value of the

209   atomic valence of ion i (V_i) divided by the valence of the strongest bond incident to it

210   ($s_{max,i}$). N_{min} is not a true coordination number (i.e., a count of nearest neighbors or

211   bonds,) but rather an expectation value of N_c, given s_{max}, for the case in which all bonds

212   are of equal strength. However, N_{min} is insensitive to cutoff distance.

213   The concept of E_n is equally problematic for models based on bond valence,

214   because if we define bond valence in terms of electric flux, it simply does not matter how

215   the valence electron density involved in a bond is distributed along the bond axis; the

216   total flux between the atomic centers stays the same (Preiser et al., 1999). This is why V_i

217   can be used rather than more realistic "partial" charges. Nevertheless, Brown and

218   Skowron (1990) have shown that cation electronegativity correlates very well with a

219   valence-based quantity called "Lewis acid strength" (L_A), which is the atomic valence of

220   the ion (V_i) divided by its average observed coordination number ($N_{t,i}$) in a large sample

221   of oxides (Eqn. 7).

222

223                                $$L_{A,i} = {V_i}/{N_{t,i}}$$ (7)

224

225   The corresponding value for anions is called "Lewis base strength," and is calculated as

226   in Eqn. 7, except that the absolute value of V_i is used. L_A provides an expectation value

227   for the average strength of the individual bonds formed, and is correlated with

228   electronegativity because it is an indicator of the electric field strength at the surface of

229   an atom (Brown and Skowron, 1990; Brown, 2011). Large cations with low charge (and

230   hence low electronegativity,) for instance, have low L_A values.

231   L_A is averaged over many structures, however, so Brown and Skowron also

232   defined an "actual Lewis acid strength", which depends on N_c of a cation in a particular

233   environment, rather than N_t, but this reintroduces the same problems with standard

234   definitions of N_c as we discussed above. In place of L_A, therefore, we simply use s_{max},

235   which is specific to individual atomic environments and does not depend on any

236   particular definition of N_c. However, s_{max} should be strongly correlated with E_n.

237   Electronic Structure Effects

238   One of the strengths of using $\|\vec{\mathbf{S}}_i\|$ to describe the distortion of coordination

239   polyhedra is that it condenses a large amount of information about the structural

240   environment into a single parameter, but by the same token, some of that information

241   cannot be extracted again. In fact, this approach is only likely to be useful for describing

242   certain types of electronic distortions. Distortions due to lone pairs and the second-order

243   Jahn-Teller (SOJT) effect tend to produce concurrent changes in $\|\vec{\mathbf{S}}_i\|$, N_{min}, and s_{max},

244   whereas the first-order Jahn-Teller (FOJT) effect usually does not.

245   In the FOJT effect, electron configurations other than d^0, d^5 (high-spin), and d^{10} in

246   transition metals can result in distortion if the strength of interaction between the d

247   subshell and the valence shell is sufficient. Gillespie and Hargittai (1991) recommended

248   adapting the VSEPR model to describe such distortions by assuming an ellipsoidal, rather

249   than spherical, electron-density distribution around the metal atom, with electron pairs

250   repelling one another to the greatest possible distances while adhering to those surfaces.

251   The ideal distribution of ligands when a metal is 4-coordinated, for instance, is

252   tetrahedral, with $\|\vec{\mathbf{S}}_i\| = 0$ v.u. But in some cases where transition metals have d^8 or d^9

253   configurations, the tetrahedral polyhedron is flattened into a disphenoidal or square-

254   planar shape. As long as the bonds all remain the same length, these distorted geometries

255   would still result in $\|\vec{S}_i\| = 0$ v.u. Also, 6-coordination ideally results in an octahedron

256   of ligands and $\|\vec{S}_i\| = 0$ v.u., but the ligands of some d^4 and d^9 transition metals instead

257   adopt a tetragonal bipyramidal configuration, also resulting in $\|\vec{S}_i\| = 0$ v.u.. In the

258   second case, there would at least be a difference in N_{min} and s_{max} between the distorted

259   and ideal geometries, but not in the first. In neither case would $\|\vec{S}_i\|$ be predictable as a

260   function of N_{min} or s_{max}.

261   The SOJT effect occurs in oxides with some d^0 (and sometimes d^1 or low-spin d^2)

262   transition metals (e.g., Zr^{4+}, Hf^{4+}, V^{4+}, V^{5+}, Nb^{5+}, Ta^{5+}, Mo^{6+}, and W^{6+},) when empty d-

263   orbitals of a cation mix with the p-orbitals of O, resulting in a large number of nearly

264   degenerate electron configurations that can be eliminated by distortion (Kaupp, 2001; Ra

265   et al., 2003; Brown, 2009; Halasyamani, 2010). In these cases, the ligands around the

266   metal often adopt configurations in which $\|\vec{S}_i\| > 0$ v.u. Kunz and Brown (1995)

267   modified the BVM to address the SOJT effect, but our approach is somewhat different.

268   Lone-pair effects produce similar distortions, and some authors even include lone-

269   pair effects on cations (e.g., Sn^{2+}, Pb^{2+}, As^{3+}, Sb^{3+}, Bi^{3+}, S^{4+}, Se^{4+}, and Te^{4+}) under the

270   SOJT heading (see Kaupp, 2001). For our purposes, we separate the two because lone-

271   pair effects on O^{2-} follow patterns similar to those affecting cations. Furthermore, the

272   above ions span a vertical trend in the p-block from the classic sp^n lone pair to

273   unhybridized s orbitals.

274   Finally, the distortion around lone-pair cations is enhanced when they are paired

275   with cations subject to SOJT distortion (Halasyamani, 2010). Therefore, we treat this as

276   a separate category.

277   Our hypothesis is that many of these types of electronic distortions will be well

278   described by $\left\lVert \vec{\mathbf{S}}_i \right\rVert$, which should usually be predictable as a function of N_{min} and/or s_{max}.

279   Methods

280   We analyzed the structural environments of the atoms in 178 simple-oxide

281   structures, with one or two cation types, with respect to bond-valence sum (S_i), the norm

282   of the valence vector sum ($\left\lVert \vec{\mathbf{S}}_i \right\rVert$), valence coordination number (N_{min}), and maximum

283   bond valence (s_{max}). All symmetrically unique atoms in these structures were treated as

284   individual data points.

285   Structures

286   Crystal structures were taken from the Crystallography Open Database

287   (http://www.crystallography.net/) and the American Mineralogist Crystal Structure

288   Database (Downs and Hall-Wallace, 2003). Structures were only chosen for analysis if

289   they were published in 1960 or later, the oxidation states of the cations were

290   unambiguous, and appropriate valence parameters (see below) were available. We also

291   did not include structures with H^+ as one of the cations, because this would have required

292   restricting ourselves to those obtained by neutron diffraction.

293   Analysis

294   Structural analysis was done with a MATLAB™ program designed to read crystal

295   structures from crystallographic information files and calculate atomic distances,

296   directions, bond valences, and valence vectors. (The program is available upon request

297   from B. R. Bickmore.)

298   We used the SoftBV valence parameters derived by Adams and coworkers

299   (Adams, 2001; Adams and Swenson, 2002; Adams et al., 2004; Adams and Rao, 2009) to

300   account for the effects of polarizability. Because of the way they are derived, each set of

301   SoftBV parameters is associated with a cutoff distance that is long enough to account for

302   very weak, secondary interactions.

303   Results and Discussion

304   Our results suggest that $\|\vec{\mathbf{S}}_i\|$ is surprisingly predictable as a function of N_{min} and

305   s_{max} for lone-pair and many SOJT distortions. In the following subsections, we report

306   these results for five groups of ions: 1) cations not expected to exhibit lone pair or SOJT

307   distortions, 2) O^{2-} ions, 3) cations with a lone pair, 4) cations expected to exhibit the

308   SOJT distortions, and 5) lone-pair cations paired with SOJT cations. Values of the

309   parameters analyzed for all atoms are reported in Table S1 (Supplementary Information).

310   Normal Cations

311   The ligands around most cations without lone pairs tend to distribute themselves

312   about the cation in a spherically symmetrical fashion. In cases where FOJT distortions

313   are expected, the distortions are often centrosymmetric. In either case, we expect valence

314   vector sums to ideally be close to zero. Our results confirm these cations tend to follow

315   the "Valence Vector Sum Postulate" (Eqn. 4) of Harvey et al. (2006), with $\|\vec{\mathbf{S}}_{Me}\| \approx 0$

316   v.u. Figure 1a plots $\|\vec{\mathbf{S}}_{Me}\|$ vs. s_{max}, showing that there is no trend, and Fig. 1b is a

317   histogram of $\|\vec{\mathbf{S}}_{Me}\|$ for these cations, showing that the values cluster around zero, with

318   an exponential distribution. The standard deviation of the $\|\vec{\mathbf{S}}_{Me}\|$ values, which is equal

319   to the mean for an exponential distribution, is 0.06 v.u.

320   One aspect of our results not addressed by Harvey et al. (2006) is that when

321    $\|\vec{\mathbf{S}}_{Me}\|$ is plotted vs. N_{min} (Figure 1c), it becomes clear that while the $\|\vec{\mathbf{S}}_{Me}\|$ values cluster

322   near zero at all values of N_{min}, the range of possible deviation decreases as N_{min} increases.

323   One likely reason for this is illustrated by Rb_2O, which has $\|\vec{\mathbf{S}}_{Me}\| = 0$ v.u., $N_{min} = 7.51$,

324   and $N_c = 4$. This is an unusual coordination environment for Rb^+, as the radius ratio of

325   cation to anion favors 12-coordination (Shannon, 1976). In this case, the average N_c of

326   the O^{2-} ions must be twice that of the Rb^+, but 24-coordinated O^{2-} ions would be

327   physically implausible, so the Rb^+ adopts a smaller coordination shell. In this situation,

328   the cations are forced into close proximity with a Rb-Rb distance of 3.37 Å, just over

329   twice the ionic radius of 1.66 Å, so any deviation from spherical symmetry in the

330   distribution of O^{2-} ligands would increase Rb-Rb repulsion (as well as O-O repulsion.)

331   Likewise, the bond-valence sum incident to Rb^+ is only 0.54 v.u., which indicates severe

332   under-bonding, but shorter Rb-O bonds would once again increase Rb-Rb and O-O

333   repulsion. Therefore, the reason for the trend in Fig. 1c may simply be that deviations

334   from spherical symmetry among ligands tend to result in more co-ion repulsion when

335   coordination numbers are higher. It may also be that the energetic cost (neglecting co-ion

336   repulsion) for deviations from $\|\vec{\mathbf{S}}_{Me}\| = 0$ v.u. varies with N_{min}, but further study is

337   needed to settle this question.

338   The essential meaning of our results for normal cations is that where the

339   coordination polyhedron is distorted about them, the distortion occurs so as to minimize

340    $\|\vec{\mathbf{S}}_{Me}\|$. The first coordination shell of Fe^{3+} in hematite (Fe_2O_3), for example, is shown in

341   Fig. 2. The cation is in distorted octahedral coordination, with two sets of three

342   equivalent bonds clustered together, one set with $s_{FeO} = 0.57$ v.u., and another with

343    $s_{FeO} = 0.38$ v.u. (A number of secondary bonds bring the valence sum on the Fe^{3+} to an

344   acceptable 2.98 v.u.) The stronger bonds repel one another, so that $\angle OFeO = 102.5°$,

345   and the weaker bonds cluster together with $\angle OFeO = 78.2°$, with the net result of

346    $\|\vec{\mathbf{S}}_{Fe}\| = 0.04$ v.u., very close to zero. As mentioned above, this result is consistent with

347   the VSEPR model, but provides a more quantitative expectation for distorted structures.

348   It is also worth noting that this sort of distortion is qualitatively required by Pauling's 4th

349   rule (Pauling, 1929).

350   We find that the compounds in which the most extreme outliers in this group are

351   found, with $\|\vec{\mathbf{S}}_{Me}\| > 0.3$ v.u., are likely metastable or unstable under ambient conditions.

352   Scrutinyite (PbO_2), for example, has $\|\vec{\mathbf{S}}_{Pb}\| = 0.47$ v.u., but is a metastable polymorph of

353   plattnerite, for which $\|\vec{\mathbf{S}}_{Pb}\| = 0$ v.u. The Cs^+ in Cs_2O has $\|\vec{\mathbf{S}}_{Cs}\| = 0.36$ v.u. and the

354   compound is hygroscopic (Earnshaw and Greenwood, 1997). Finally, $\|\vec{\mathbf{S}}_{Al}\| = 0.31$ v.u.

355   for one of the Al^{3+} ions in κ-Al_2O_3, which is a metastable, nanophase polymorph of

356   corundum. One of the B^{3+} ions in diomignite ($Li_2B_4O_7$) has $\|\vec{\mathbf{S}}_B\| = 0.10$ v.u., which is

357   within two standard deviations of zero, while the other has $\|\vec{\mathbf{S}}_B\| = 0.76$ v.u. Diomignite

358   forms from spodumene fluid inclusions, crystallizing from incompatible elements during

359   the late stages of pegmatite formation (London et al., 1987), so it is not likely to be stable

360   under ambient conditions. The same seems to be true for compounds incorporating

361   cations with $\|\vec{\mathbf{S}}_{Me}\|$ values considerably less than 0.3, but there are too many of them to

362   discuss here.

363   O^{2-} Ions

364   The coordination geometries of anions are often less symmetrical, because lone

365   pairs are typically involved. O^{2-} ions, for example, have 8 valence electrons, so unless N_c

366   > 4 they are expected to have 4 total electron pairs, including bonded and lone pairs.

367   VSEPR predicts that bond angles about a central O^{2-} ion will be close to the ideal

368   tetrahedral angle of 109.5°, but may deviate from this due to ligand-ligand repulsion and

369   differences in how effectively particular electron pairs repel others, which depends on the

370   strength and electronegativity of the bonds (Gillespie and Hargittai, 1991). When $N_c > 4$,

371   the ligands are expected to distribute themselves as symmetrically as possible around the

372   central O^{2-}.

373   Figure 3a shows $\|\vec{\mathbf{S}}_O\|$ plotted vs. s_{max} for the O^{2-} ions. Most of the data points in

374   Fig. 3a lie around the thick, solid line, which was determined as follows. If all the bonds

375   incident to the O^{2-} ion are of equal strength, then $s_{max} = 0.5$ v.u. implies $N_{min} = 4$, $s_{max} =$

376   2 v.u. implies $N_{min} = 1$, and $s_{max} < 0.5$ v.u. implies $N_{min} > 4$ (Eqn. 6). Where $N_{min} \geq 4$, it is

377   expected that $\|\vec{\mathbf{S}}_O\| = 0$ v.u., and if the valence-sum rule (Eqn. 3) is obeyed then

378    $\|\vec{\mathbf{S}}_O\| = 2$ v.u. for $N_{min} = 1$. Connection of these theoretically constrained values results

379   in the line in Fig. 3a. Eqns. 8-9 describe the two segments of the line.

380

381    $$\|\vec{\mathbf{S}}_O\| = {}^4/_3\, s_{max} - {}^2/_3 \qquad \text{v.u.} \quad (1 \leq N_{min} \leq 4) \qquad (8)$$

382    $$\|\vec{\mathbf{S}}_O\| = 0 \text{ v.u.} \qquad\qquad (N_{min} > 4) \qquad\qquad (9)$$

383

384   The dotted line in Fig. 3a denotes $\|\vec{\mathbf{S}}_O\| = s_{max}$, and where $s_{max} > 1.5$ v.u., $\|\vec{\mathbf{S}}_O\|$

385   tends to fall along this line. This occurs in cases where a single, strong bond accounts for

386   almost all the bond valence incident to the O^{2-} ion, and when the strength of this bond is

387   less than 2 v.u., steric constraints can prevent other bonds from taking up the remaining

388   valence on the O^{2-}, and hence lowering $\|\vec{\mathbf{S}}_O\|$, as well.

389   In Fig. 3b, we have plotted $\|\vec{\mathbf{S}}_O\|$ vs. N_{min} for the O^{2-} ions, and the thick, solid line

390   described by Eqns 8-9 is transformed via Eqn. 6 and reproduced there. The thin, dashed

391   line represents the $\|\vec{\mathbf{S}}_O\|$ values expected if we enforce the valence-sum rule (Eqn. 3) and

392   tetrahedral (109.5°) bond angles.   Where $1 < N_{min} < 4$, the $\|\vec{\mathbf{S}}_O\|$ values generally fall

393   below the dashed line, and this is for three reasons. First, only very covalent bonds can

394   be as strong as 2 v.u., and as N_{min} increases, the bonds generally become more ionic (i.e.,

395   the electronegativity of the cations decreases.) Where the electronegativity of the ligands

396   is less, the electron density in the bonded pairs is closer to the central atom, and they take

397   up more space on the central atom's surface, causing the bond angles to increase

398   (Gillespie and Hargittai, 1991). Larger bond angles lead to decreased values of $\|\vec{\mathbf{S}}_O\|$,

399   relative to what would be expected with ideal tetrahedral angles.

400   The intermediate values along the solid line in Fig. 3b are also of interest. For

401   instance, if the strengths of all bonds are equal and the valence-sum rule is obeyed, then

402      $s_{max} = 1$ v.u. implies $N_{min} = 2$, and Eqn. 8 predicts $\|\vec{\mathbf{S}}_O\| = 0.67$ v.u., which corresponds

403   to $\angle MeOMe = 141°$. In the SiO_2 polymorphs, $\angle SiOSi$ is typically in the range 140-

404   145°, with some notable exceptions discussed below. Given the same assumptions, s_{max}

405      $= 0.67$ v.u. for $N_{min} = 3$, and Eqn. 8 predicts $\|\vec{\mathbf{S}}_O\| = 0.23$ v.u., which is exactly the value

406   obtained for O^{2-} in the rutile (TiO_2) structure (see Table 1).

407   Fig. 3c shows a histogram of $\Delta\|\vec{\mathbf{S}}_O\|$, defined as the deviation of $\|\vec{\mathbf{S}}_O\|$ from Eqns.

408   8-9. The distribution has a mean value of -0.03 v.u., standard deviation of ±0.16 v.u.,

409   skewness of 0.62, and kurtosis of 8.24. This indicates that the distribution is centered

410   very close to zero, more peaked than the normal distribution and moderately skewed

411   toward positive values. Where chemical data are available, it seems that outliers with

412   deviations greater than 0.5 v.u. are all metastable or unstable under ambient conditions,

413   or exhibited bonding types not addressed by the BVM. An O^{2-} in kamiokite ($Fe_2Mo_3O_8$),

414   for instance, has $\Delta\|\vec{\mathbf{S}}_O\| = 1.10$ v.u., but this strange structure exhibits strong Mo-Mo

415   bonds (Kanazawa and Sasaki, 1986). One O^{2-} in diomignite ($Li_2B_4O_7$) (discussed above)

416   has $\Delta\|\vec{\mathbf{S}}_O\| = 0.54$ v.u. An O^{2-} in tridymite, a high-temperature polymorph of quartz

417   (SiO_2) has $\Delta\|\vec{\mathbf{S}}_O\| = -0.72$ v.u., while another in coesite, a high-pressure quartz

418   polymorph has $\Delta\|\vec{\mathbf{S}}_O\| = -0.71$ v.u. WO_3 has one O^{2-} with $\Delta\|\vec{\mathbf{S}}_O\| = 0.54$ v.u., but is

419   unique among oxides of the elements in that it has at least seven polymorphs and can

420   easily undergo numerous crystallographic transformations near ambient conditions

421   (Earnshaw and Greenwood, 1997).

422   Cations—Lone Pair

423   Cations having a lone pair or filled valence s-subshell (Sn^{2+}, Pb^{2+}, As^{3+}, Sb^{3+},

424   Bi^{3+}, S^{4+}, Se^{4+}, and Te^{4+}) range in atomic valence from +2 to +4, and vary widely in ionic

425   radius, and yet the behavior of $\|\vec{\mathbf{S}}_{Me}\|$ with respect to N_{min} and s_{max} for these cations is

426   surprisingly uniform. Figs. 4a and 4b plot $\|\vec{\mathbf{S}}_{Me}\|$ vs. s_{max} and N_{min}, respectively, and

427   different symbols are used to denote different cations. In Fig. 4b, it is clear that around

428   $N_{min} \approx 3\text{-}4$ the slope of the trend abruptly becomes more steep, while it is more shallow

429   for $N_{min} > 4$. By comparison with Fig. 4a, we can see that in this region, small changes in

430   s_{max} lead to large changes in $\|\vec{\mathbf{S}}_{Me}\|$ but small changes in N_{min}. These separate trends will

431   become clearer when we compare distortions involving the SOJT effect.

432   The origin of the two distinct trends in Fig. 4b may simply be geometric—i.e.,

433   distortion of coordination polyhedra with larger numbers of ligands may naturally result

434   in smaller changes in $\|\vec{S}_{Me}\|$. In that case, it seems difficult to explain the consistency of

435   the slope for $N_{min} > 4$, and the rather abrupt transition in slope for $N_{min} \approx$ 3-4.

436   These trends may also originate with differences in the electronic structure effects

437   involved. To this point, we have been calling any cation with an unbonded valence

438   electron pair a "lone-pair cation," but it has traditionally been held that a "lone-pair" is

439   formed due to s-p hybridization in the valence shell, which may not be the right

440   explanation for the distortion around all of the cations discussed here. Some electronic

441   structure studies have concluded that distortion around Pb^{2+} in oxides, for example, is due

442   to s-p hybridization in the valence shell, but these studies have often used density

443   functional theory (DFT) with the lanl2DZ+d basis, which uses a large, 78 core e^-

444   effective core potential (ECP). Wander and Clark (2008) showed that a basis set (aug-cc-

445   pvdz-PP) using a smaller, 60 core e^- ECP produces very different results. That is, aug-cc-

446   pvdz-PP results in less distorted Pb^{2+} coordination environments, and this distortion does

447   not appear to be caused by s-p hybridization in the valence shell. Instead, the ligands

448   seem to be arranged in orientations roughly corresponding to those of the natural Pb $6p$

449   and $5d$ orbitals.

450   Fig. 4c plots $\|\vec{S}_{Me}\|$ vs. N_{min} for the Pb^{2+} ions in the crystal structures analyzed

451   here, along with $Pb^{2+} \cdot (H_2O)_{1-9}$ structures optimized by Wander and Clark (2008) using

452   both lanl2DZ+d (Large Core DFT) and aug-cc-pvdz-PP (Small Core DFT) basis sets.

453   The lanl2DZ+d calculations would not allow more than 5 H_2O molecules to directly bond

454   to the central Pb^{2+}, but larger N_c values were possible with the aug-cc-pvdz-PP

455   calculations. Both sets of calculated structures plot within essentially the same range

456   covered by the crystal structures, but the ranges of the calculated structures do not

457   overlap with each other ($N_{min} \approx$ 3-4 for lanl2DZ+d and $N_{min} > 4$ for aug-cc-pvdz-PP.) It is

458   intriguing that the lanl2DZ+d structures plot in the region where both trends on Fig. 4b

459   overlap, while the aug-cc-pvdz-PP structures plot exclusively along the trend for $N_{min} > 4$.

460   This behavior is consistent with the hypothesis that the structures in the $N_{min} \approx$ 3-4 trend

461   distort via *s-p* hybridization in the valence shell, while those in the $N_{min} > 4$ trend distort

462   via the other mechanism identified by Wander and Clark (2008). Indeed, most of the

463   points along the $N_{min} > 4$ trend in Fig. 4b represent Pb^{2+} and Bi^{3+}, which are both Period 6

464   elements, and this may simply represent the general behavior of the *p*-block elements in

465   this region of the Periodic Table. This conjecture is supported by the results of Ayala et

466   al. (2008), who recently calculated Po^{4+} hydrated structures using DFT and a small-core

467   basis set, and obtained coordination-shell distortions very similar to those found by

468   Wander and Clark (2008) for Pb^{2+}. The only other points clearly belonging to the $N_{min} >$

469   4 trend represent a single Sn^{2+} from SnO and a single Te^{4+} from paratellurite. Both are

470   Period 5 *p*-block elements, and in fact, there are several other Te^{4+} data points from other

471   structures well within the $N_{min} \approx$ 3-4 trend. Therefore, it may be that *p*-block elements

472   from Periods 5-6 are capable of both types of distortion mechanisms, depending on the

473   coordination number, but further electronic structure calculations are needed to establish

474   this conjecture.

475   Cations—SOJT

476   Cations expected to be subject to the SOJT effect (Hf^{4+}, Mo^{6+}, Nb^{5+}, Ta^{5+}, V^{4+},

477   V^{5+}, W^{6+}, Zr^{4+}) exhibit distortions similar to cations with a lone pair, but to a lesser

478   extent. Figs. 5a and 5b plot $\|\vec{\mathbf{S}}_{Me}\|$ vs. s_{max} and N_{min}, respectively, for the SOJT cations,

479   and the lone-pair cations are plotted there for comparison. Fig. 5a shows that the $\|\vec{\mathbf{S}}_{Me}\|$

480   distortion response of the SOJT cations to s_{max} is different for each cation, but the order

481   roughly follows the cation valence. That is, SOJT cations with higher valence tend to

482   distort less, given the same s_{max}, as s_{max} is a smaller share of the total bond valence

483   incident to higher-valence cations. These separate trends disappear in Fig. 5b, because

484   N_{min} takes the cation valence into account. Here, the SOJT cations seem to fall roughly

485   along the same trend as the lone-pair cations for $N_{min} \approx$ 3-4, although the $\|\vec{\mathbf{S}}_{Me}\|$ values

486   for SOJT cations with $N_{min} > 4$ fall somewhat lower than their counterparts among the

487   lone-pair cations, with $\|\vec{\mathbf{S}}_{Me}\| = 0$ v.u. at $N_{min} \approx 6$, rather than $N_{min} \approx 8$.

488   In Fig. 5b, we have also plotted lines indicating the three trends just mentioned.

489   Line 1 is followed by both the lone-pair cations and SOJT cations around $N_{min} \approx$ 3-4, and

490   seems to trace the distortion of a tetrahedral coordination shell toward a trigonal-

491   pyramidal geometry. Here, large changes in $\|\vec{\mathbf{S}}_{Me}\|$ result from small changes in N_{min}.

492   Lines 2 and 3 trace the distortion of SOJT and lone-pair cation coordination polyhedra,

493   respectively, with $N_{min} > 4$. Line 2 traces the distortion of octahedral coordination around

494   SOJT cations until it merges with the tetrahedral distortion trend, while Line 3 traces the

495   distortion of 8-coordination around lone-pair cations until it also merges with the

496   tetrahedral distortion trend. In cases where N_{min} is greater than the x-intercepts for Lines

497   2 and 3, $\|\vec{\mathbf{S}}_{Me}\| = 0$ v.u.

498   Given the previous discussion of the trends marked by Lines 1 and 3 for lone-pair

499   cations, it seems probable that the SOJT distortions marked by Lines 1 and 2 have similar

500   origins in distinct electronic structure effects. Further research will test this hypothesis.

501   Cations—Lone Pair, Combined with SOJT Cation

502   Distortion of coordination polyhedra around lone-pair cations can be altered when

503   they are paired with cations subject to SOJT distortion in oxides (Halasyamani, 2010).

504   Figs. 6a and 6b show $\|\vec{\mathbf{S}}_{Me}\|$ vs. s_{max} and N_{min}, respectively, for lone-pair cations, SOJT

505   cations, and lone-pair cations paired with SOJT cations. (The last category is divided by

506   individual cation type.) Most of the cations in the latter category appear along the same

507   trends as the other lone-pair cations, but a few of them lie along the SOJT cation trends or

508   intermediate between the lone-pair and SOJT trends. Although the sample is small, it

509   may be worth noting that only some of the Pb^{2+} ions seem to have been affected in this

510   way, while the Bi^{3+}, Sb^{3+}, and Sn^{2+} ions seem to behave similarly to the other lone-pair

511   cations.

512   Concluding Remarks

513   Our hypothesis that $\|\vec{\mathbf{S}}_O\|$ should be predictable as a function of s_{max} and N_{min} for

514   the types of electronic structure effects discussed here turns out to be true to a surprising

515   degree. In fact, $\|\vec{\mathbf{S}}_O\|$ follows predictable, but distinct trends for ions subject to different

516   types of electronic structure effects. These results suggest that $\|\vec{\mathbf{S}}_O\|$ is indeed a

517   "common currency," in that it seems to mean roughly the same thing across a number of

518   contexts. In the case of lone-pair effects on O^{2-} coordination geometry, $\|\vec{\mathbf{S}}_O\|$ can be

519   approximately predicted, given only the valence of the strongest bond incident to it, even

520   though different numbers of lone pairs are involved. In the case of distortion around

521   cations with a single lone pair, $\|\vec{\mathbf{S}}_O\|$ follows a fairly well defined trend with respect to

522   s_{max} and N_{min}, even though the cations have oxidation states ranging from +2 to +4. The

523   trends followed by $\|\vec{\mathbf{S}}_O\|$ values for SOJT cations are more complex, but still quite

524   consistent among different cations in the category.

525   Why should $\|\vec{\mathbf{S}}_O\|$ be so transferable in this context? As discussed above, bond

526   valence is related to the factors assumed to control molecular geometry in the VSEPR

527   model. Gibbs and coworkers (Gibbs et al., 2001; Gibbs et al., 2003; Gibbs et al., 2004),

528   for instance, have used quantum mechanical calculations to show that bond valence

529   varies linearly with the electron density at bond-critical points, which implies that bond

530   valence really is a good measure of bond order. Since the VSEPR model posits that the

531   space taken up on the surface of an atom by bonded electron pairs depends partially on

532   bond order, it is reasonable to suppose that bonds of a given valence take up a fairly

533   consistent amount of space. The VSEPR model also posits that the electronegativity of

534   ligands relative to the central atom affects the amount of space that bonded pairs take up

535   at the surface of the central atom. As noted above, expectation values for bond valences

536   between various cations and O^{2-} (see Eqn. 7) are highly correlated with cation

537   electronegativity (Brown and Skowron, 1990).

538   Supposing it is possible to estimate an ideal value for $\|\vec{\mathbf{S}}_O\|$ in a given structural

539   context (e.g., with Eqns. 8-9,) it may be that deviation from that ideal value is a plausible

540   proxy for some aspects of structural potential energy. Although interpretation of

541   deviations from ideal $\|\vec{\mathbf{S}}_O\|$ values is complicated by other structural factors, such as

542   deviation from ideal valence sums and non-bonded interactions, our results indicate that

543   large deviations inevitably entail some energetic cost, as the outliers we identified are all

544   unstable or metastable under ambient conditions.

545   Nevertheless, accurately estimating ideal $\|\vec{\mathbf{S}}_O\|$ values may or may not require

546   further characterization. Compare, for instance, quartz (SiO_2) and isostructural GeO_2. In

547   both cases, the strongest bonds incident to the O^{2-} ions are 1.01 v.u., which implies

548    $\|\vec{\mathbf{S}}_O\| = 0.68$ given Eqn. 8, which is equivalent to $\angle MeOMe = 141°$. These are close to

549   the values obtained for quartz ($\|\vec{\mathbf{S}}_O\| = 0.62$ v.u., $\angle SiOSi = 143.6°$), but somewhat

550   different from those for quartz-like GeO_2 ($\|\vec{\mathbf{S}}_O\| = 0.82$ v.u., $\angle GeOGe = 130.1°$). It may

551   be that ideal $\|\vec{\mathbf{S}}_O\|$ values for O^{2-} ions attached to Si^{4+} ligands should be smaller than

552   those for O^{2-} ions attached to Ge^{4+} ligands. However, non-bonded forces might also

553   come into play; e.g., Ge is larger and more polarizable than Si, which would make Ge-Ge

554   van der Waals forces more attractive (Cambi et al., 1991; Rappé et al., 1992).

555   Research is ongoing to address such questions, but for now it is sufficient to note

556   that the VBVM has already proven to be a useful extension of bond-valence theory for

557   predicting certain structural features in crystals, and we have shown that it is possible to

558   extend its usefulness to atoms where electronic distortions play a role in determining

559   molecular geometry. Therefore, we now have a bond-valence-based framework for

560   predicting both acceptable combinations of bond lengths and their spatial distribution

561   about every atom in many crystals.

562

References

568

569   Adams, S. (2001) Relationship between bond valence and bond softness of alkali halides

570   and chalcogenides. Acta Crystallographica, B57, 278-287.

571   Adams, S. and Swenson, J. (2002) Bond valence analysis of transport pathways in RMC

572   models of fast ion conducting glasses. Physical Chemistry Chemical Physics, 4,

573   3179-3184.

574   Adams, S. and Rao, R.P. (2009) Transport pathways for mobile ions in disordered solids

575   from the analysis of energy-scaled bond-valence mismatch landscapes. Physical

576   Chemistry Chemical Physics, 11, 3210-3216.

577   Adams, S., Moretzki, O., and Canadell, E. (2004) Global instability index optimizations

578   for the localization of mobile protons. Solid State Ionics, 168, 281-290.

579   Angel, R.J., Zhao, J., and Ross, N.L. (2005a) General rules for predicting phase

580   transitions in perovskites due to octahedral tilting. Physical Review Letters, 95,

581   025503.

582   Angel, R.J., Ross, N.L., and Zhao, J. (2005b) The compression of framework minerals:

583   Beyond rigid polyhedra. European Journal Of Mineralogy, 17, 193-199.

584   Ayala, R., Martinez, J.M., Pappalardo, R.R., Muñoz-Paez, A., and Marcos, E.S. (2008)

585   Po(IV) hydration: A quantum chemical study. Journal of Physical Chemistry,

586   B112, 5416-5422.

587   Bickmore, B.R., Rosso, K.M., Brown, I.D., and Kerisit, S. (2009) Bond-valence

588   constraints on liquid water structure. Journal of Physical Chemistry, A113, 1847-

589   1857.

590   Bickmore, B.R., Tadanier, C.J., Rosso, K.M., Monn, W.D., and Eggett, D.L. (2004)

591   Bond-valence methods for pK_a prediction: Critical reanalysis and a new

592   approach. Geochimica et Cosmochimica Acta, 68, 2025-2042.

593   Bickmore, B.R., Rosso, K.M., Tadanier, C.J., Bylaska, E.J., and Doud, D. (2006) Bond-

594   valence methods for pKa prediction. II. Bond-valence, electrostatic, molecular

595   geometry, and solvation effects. Geochimica et Cosmochimica Acta, 70, 4057-

596   4071.

597   Brown, I.D. (1988) What factors determine cation coordination numbers? Acta

598   Crystallographica, B44, 545-553.

599   Brown, I.D. (2002) The Chemical Bond in Inorganic Chemistry: The bond valence

600   model, 278 p. Oxford University Press, New York.

601   Brown, I.D. (2009) Recent developments in the methods and applications of the bond

602   valence model. Chemical Reviews, 109, 6858-6919.

603   Brown, I.D. (2011) View of lone electron pairs and their role in structural chemistry.

604   Journal of Physical Chemistry, A115, 12638-12645.

605   Brown, I.D. and Altermatt, D. (1985) Bond-valence parameters obtained from a

606   systematic analysis of the inorganic crystal structure database. Acta

607   Crystallographica, B41, 244-247.

608   Brown, I.D. and Skowron, A. (1990) Electronegativity and Lewis acid strength. Journal

609   of the American Chemical Society, 112, 3401-3403.

610   Brown, T.L. (2003) Making Truth: Metaphor in science, 215 p. University of Illinois

611   Press, Urbana.

612   Cambi, R., Cappelletti, D., Liuti, G., and Pirani, F. (1991) Generalized correlations in

613   terms of polarizability for van der Waals interaction potential parameter

614   calculations. Journal of Chemical Physics, 95, 1852-1861.

615   Cooper, V.R., Grinberg, I., and Rappe, A.M. (2003) Extending first principles modeling

616   with crystal chemistry: A bond-valence based classical potential. In P.K. Davies

617   and D.J. Singh, Eds., Fundamental Physics of Ferroelectrics. American Institute

618   of Physics, Melville, New York.

619   Downs, R.T. and Hall-Wallace, M. (2003) The American Mineralogist Crystal Structure

620   Database. American Mineralogist, 88, 247-250.

621   Earnshaw, A. and Greenwood, N. (1997) Chemistry of the Elements, 1600 p.

622   Butterworth-Heinemann, Waltham, MA.

623   Gibbs, G.V., Cox, D.F., and Rosso, K.M. (2004) A connection between empirical bond

624   strength and the localization of the electron density at the bond critical points of

625   the SiO bonds in silicates. Journal of Physical Chemistry, A108, 7643-7645.

626   Gibbs, G.V., Boisen, M.B., Beverly, L.L., and Rosso, K.M. (2001) A computational

627   quantum chemical study of the bonded interactions in Earth materials and

628   structurally and chemically related molecules. Reviews in Mineralogy and

629   Geochemistry, 42, 345-381.

630   Gibbs, G.V., Rosso, K.M., Cox, D.F., and Boisen Jr., M.B. (2003) A physical basis for

631   Pauling's definition of bond strength. Physics and Chemistry of Minerals, 30, 317-

632   320.

633   Gillespie, R.J. and Hargittai, I. (1991) The VSEPR Model of Molecular Geometry, 248 p.

634   Allyn and Bacon, Boston.

635   Grinberg, I., Cooper, V.R., and Rappe, A.M. (2002) Relationship between local structure

636   and phase transitions of a disordered solid solution. Nature, 419, 909-911.

637   Grinberg, I., Cooper, V.R., and Rappe, A.M. (2004) Oxide chemistry and local structure

638   of $PbZr_xTi_{1-x}O_3$ studied by density-functional theory supercell calculations.

639   Physical Review B, 69, 144118.

640   Halasyamani, P.S. (2010) Noncentrosymmetric inorganic oxide materials: Synthetic

641   strategies and characterisation techniques. In D.W. Bruce, D. O'Hare, and R.I.

642   Walton, Eds., Functional Oxides. Wiley, Chichester.

643   Harvey, M.A., Baggio, S., and Baggio, R. (2006) A new simplifying approach to

644   molecular geometry description: the vectorial bond-valence model. Acta

645   Crystallographica, B62, 1038-1042.

646   Hiemstra, T., Venema, P., and Van Riemsdijk, W.H. (1996) Intrinsic proton affinity of

647   reactive surface groups of metal (hydr)oxides: The bond valence principle.

648   Journal of Colloid and Interface Science, 184, 680-692.

649   Kanazawa, Y. and Sasaki, A. (1986) Structure of Kamiokite. Acta Crystallographica,

650   C42, 9-11.

651   Kaupp, M. (2001) "Non-VSEPR" structures and bonding in d^0 systems. Angewandte

652   Chemie International Edition, 40, 3534-3565.

653   Kunz, M. and Brown, I.D. (1995) Out-of-center distortions around octahedrally

654   coordinated d^0 transition metals. Journal of Solid State Chemistry, 115, 395-406.

655   London, D., Zolensky, M.E., and Roedder, E. (1987) Diomignite: Natural $Li_2B_4O_7$ from

656   the Tanco pegmatite, Bernic Lake, Manitoba. Canadian Mineralogist, 25, 173-

657   180.

658   Lufaso, M.W. and Woodward, P.M. (2001) Prediction of the crystal structures of

659   perovskites using the software program SPuDS. Acta Crystallographica, B57,

660   725-738.

661   Müller, P., Köpke, S., and Sheldrick, G.M. (2003) Is the bond-valence method able to

662   identify metal atoms in protein structures? Acta Crystallographica, D59, 32-37.

663   Müller, U. (2007) Inorganic Structural Chemistry, 268 p. Wiley, Chichester, UK.

664   Pauling, L. (1929) The principles determining the structure of complex ionic crystals.

665   Journal of the American Chemical Society, 51, 1010-1026.

666   Perez-Mato, J.M., Withers, R.L., Larsson, A.-K., Orobengoa, D., and Liu, Y. (2009)

667   Distortion modes and related ferroic properties of the stuffed tridymite-type

668   compounds $SrAl_2O_4$ and $BaAl_2O_4$. Physical Review, B79, 064111.

669   Preiser, C., Lösel, J., Brown, I.D., Kunz, M., and Skowron, A. (1999) Long-range

670   Coulomb forces and localized bonds. Acta Crystallographica, B55, 698-711.

671   Ra, H.-S., Ok, K.M., and Halasyamani, P.S. (2003) Combining second-order Jahn-Teller

672   distorted cations to create highly efficient SHG materials: Synthesis,

673   characterization, NLO properties of $BaTeM_2O_9$ (M = M^{6+} or W^{6+}. Journal of the

674   American Chemical Society, 125, 7764-7765.

675   Rappé, A.K., Casewit, C.J., Colwell, K.S., Goddard, W.A.I., and Skiff, W.M. (1992)

676   UFF, a full periodic table force field for molecular mechanics and molecular

677   dynamics simulations. Journal of the American Chemical Society, 114, 10024-

678   10035.

679   Salinas-Sanchez, A., Garcia-Muñoz, J.L., Rodriguez-Carvajal, J., Saez-Puche, R., and

680   Martinez, J.L. (1992) Structural characterization of R_2BaCuO_5 (R=Y, Lu, Yb,

681   Tm, Er, Ho, Dy, Gd, Eu and Sm) oxides by X-ray and neutron diffraction. Journal

682   of Solid State Chemistry, 100, 201-211.

683   Shannon, R.D. (1976) Revised effective ionic radii and systematic studies of interatomic

684   distances in halides and chalcogenides. Acta Crystallographica, A32.

685   Shin, Y.-H., Cooper, V.R., Grinberg, I., and Rappe, A.M. (2005) Development of a bond-

686   valence molecular-dynamics model for complex oxides. Physical Review B, 71,

687   No. 054104.

688   Wander, M.C.F. and Clark, A.E. (2008) Hydration properties of aqueous Pb(II) ion.

689   Inorganic Chemistry, 47, 8233-8241.

690   Zhao, J., Ross, N.L., and Angel, R.J. (2004a) New view of the high-pressure behaviour of

691          $GdFeO_3$-type perovskites. Acta Crystallographica, B60, 263-271.

692   Zhao, J., Ross, N.L., and Angel, R.J. (2004b) Polyhedral control of the rhombohedral to

693   cubic phase transition in $LaAlO_3$ perovskite. Journal of Physics: Condensed

694   Matter, 16, 8763-8773.

695   Zhao, J., Ross, N.L., and Angel, R.J. (2006) Estimation of polyhedral compressibilities

696   and structural evolution of $GdFeO_3$-type perovskites at high pressures. Acta

697   Crystallographica, B62, 431-439.

698

699

700   Figure Captions

701   **Figure 1.** a) $\|\vec{\mathbf{S}}_{Me}\|$ vs. s_{max} for cations not subject to electronic distortions, showing that

702   there is no trend. b) Histogram of $\|\vec{\mathbf{S}}_{Me}\|$ for these cations, showing that the values

703   cluster around zero. c) $\|\vec{\mathbf{S}}_{Me}\|$ vs. N_{min} for the same group of cations.

704

705   **Figure 2.** The coordination polyhedron of Fe^{3+} in hematite shows how distortion of the

706   polyhedron occurs in such a way as to minimize $\|\vec{\mathbf{S}}_O\|$. In this case, the octahedron is

707   distorted with one set of three weaker bonds, and another set of three stronger bonds.

708   The bond angles show that the weaker bonds bunch together, while the stronger bonds

709   are repelled from one another. The net result is $\|\vec{\mathbf{S}}_{Fe}\| = 0.04$ v.u.

710

711   **Figure 3.** a) $\|\vec{\mathbf{S}}_i\|$ vs. s_{max} for the O^{2-} ions. The thick, solid line represents Eqns. 8-9,

712   while the dotted line denotes $\|\vec{\mathbf{S}}_O\| = s_{max}$. b) $\|\vec{\mathbf{S}}_O\|$ vs. N_{min} for the O^{2-} ions. The thick,

713   solid line represents Eqns 8-9, transformed via Eqn. 6. The dotted line represents the

714    $\|\vec{\mathbf{S}}_O\|$ values expected if we enforce the valence-sum rule (Eqn. 3) and tetrahedral

715   (109.5°) bond angles. c) Histogram of $\Delta\|\vec{\mathbf{S}}_O\|$, defined as the deviation of $\|\vec{\mathbf{S}}_O\|$ from

716   Eqns. 8-9.

717

718   **Figure 4.** $\|\vec{\mathbf{S}}_{Me}\|$ vs. a) s_{max} and b) N_{min}, for cations with one lone pair. c) The $\|\vec{\mathbf{S}}_{Me}\|$ vs.

719   N_{min} values for Pb^{2+} ions in the crystals are re-plotted here, along with the values for

720    $Pb^{2+} \cdot (H_2O)_{1-9}$ structures optimized by Wander and Clark (2008) using both lanl2DZ+d

721   (Large Core DFT) and aug-cc-pvdz-PP (Small Core DFT) basis sets.

722

723   **Figure 5.** $\|\vec{\mathbf{S}}_{Me}\|$ vs. a) s_{max} and b) N_{min}, for cations subject to SOJT effects. Values for

724   cations with a lone pair (see Fig. 4) are plotted for comparison.

725

726   **Figure 6.** $\left\|\vec{\mathbf{S}}_{Me}\right\|$ vs. a) s_{max} and b) N_{min}, for cations with a lone pair that are paired with

727   cations subject to SOJT effects. Values for other cations with a lone pair (see Fig. 4) and

728   those for cations subject to SOJT effects (see Fig. 5) are plotted for comparison.
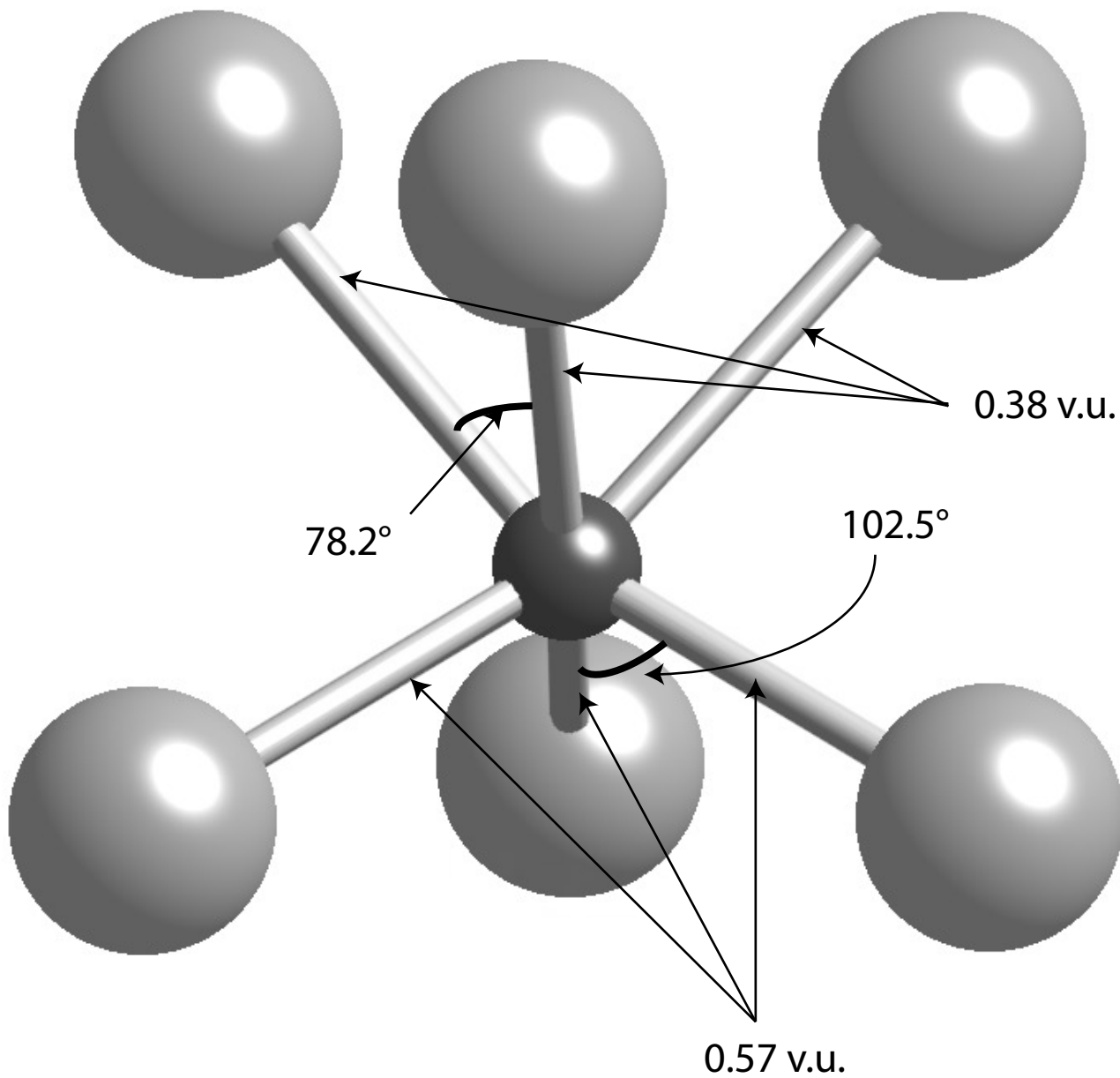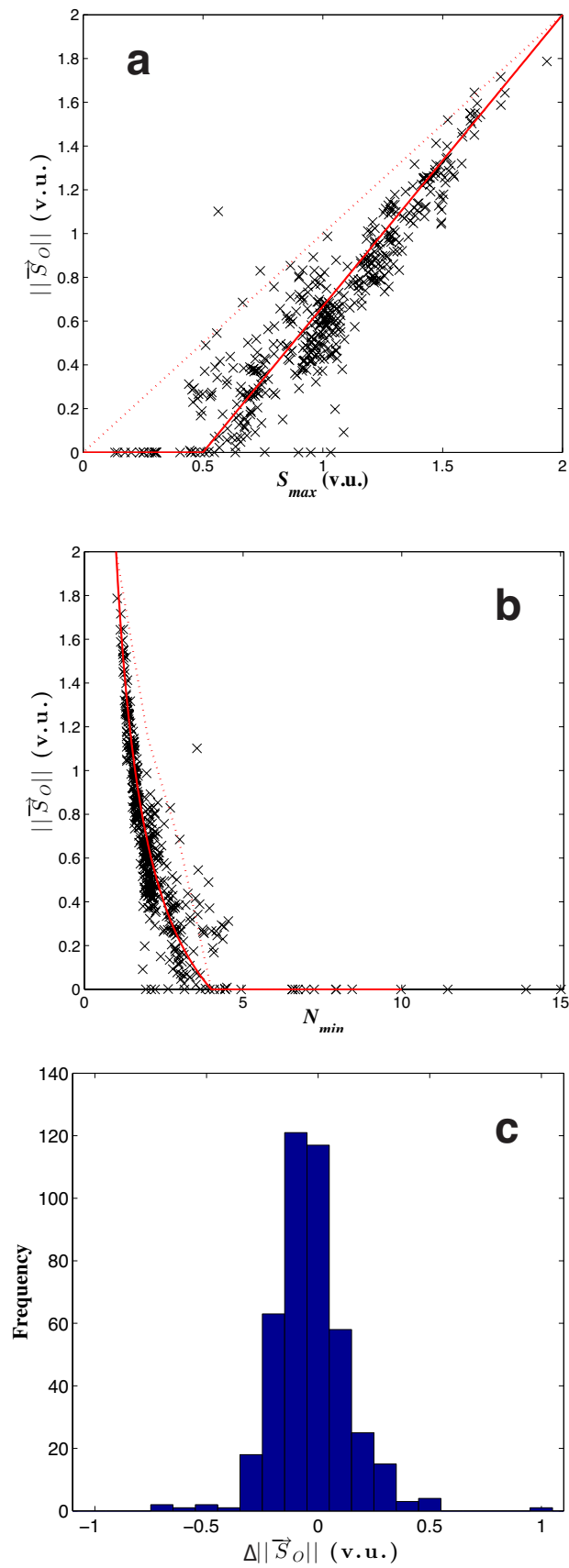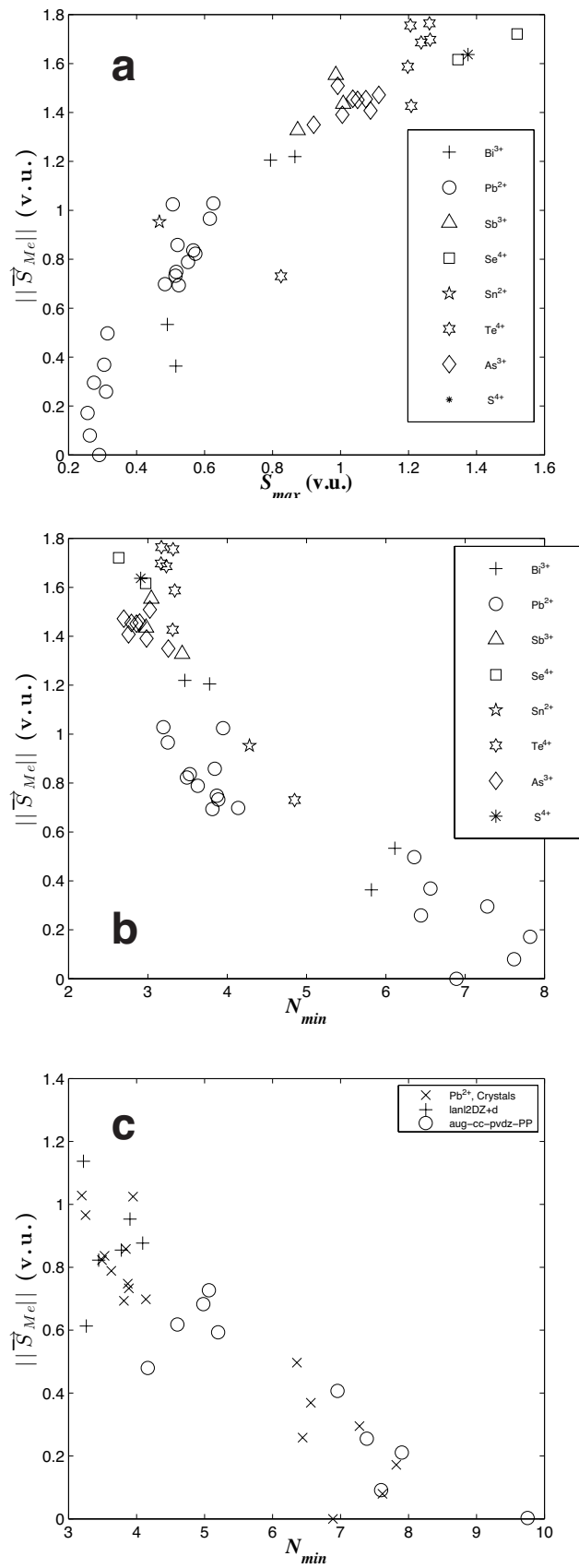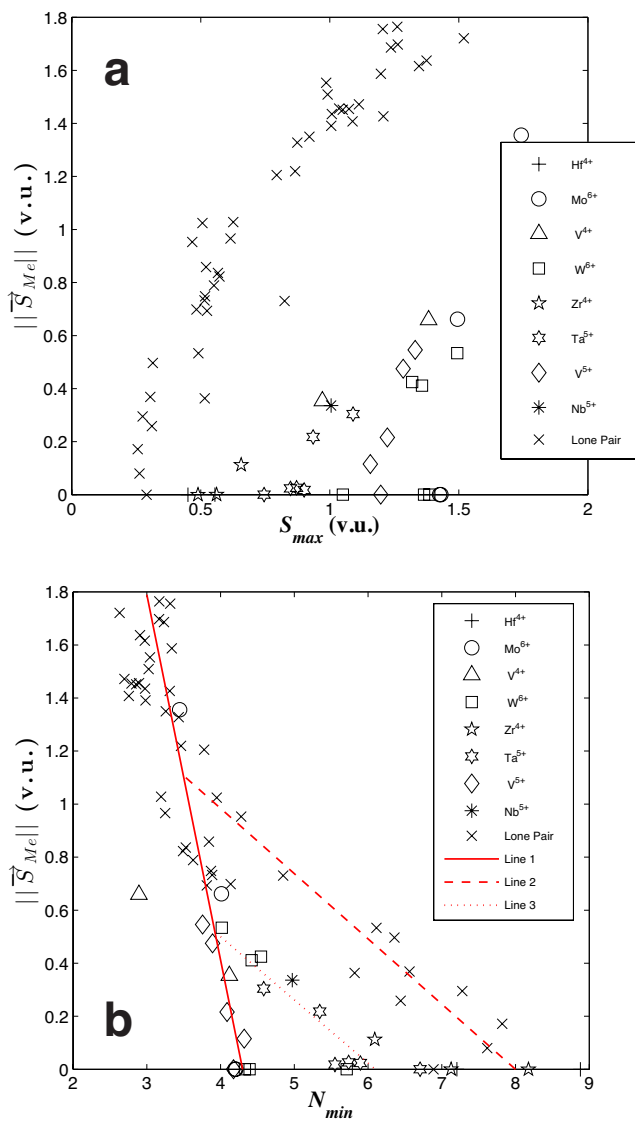
Figure 1
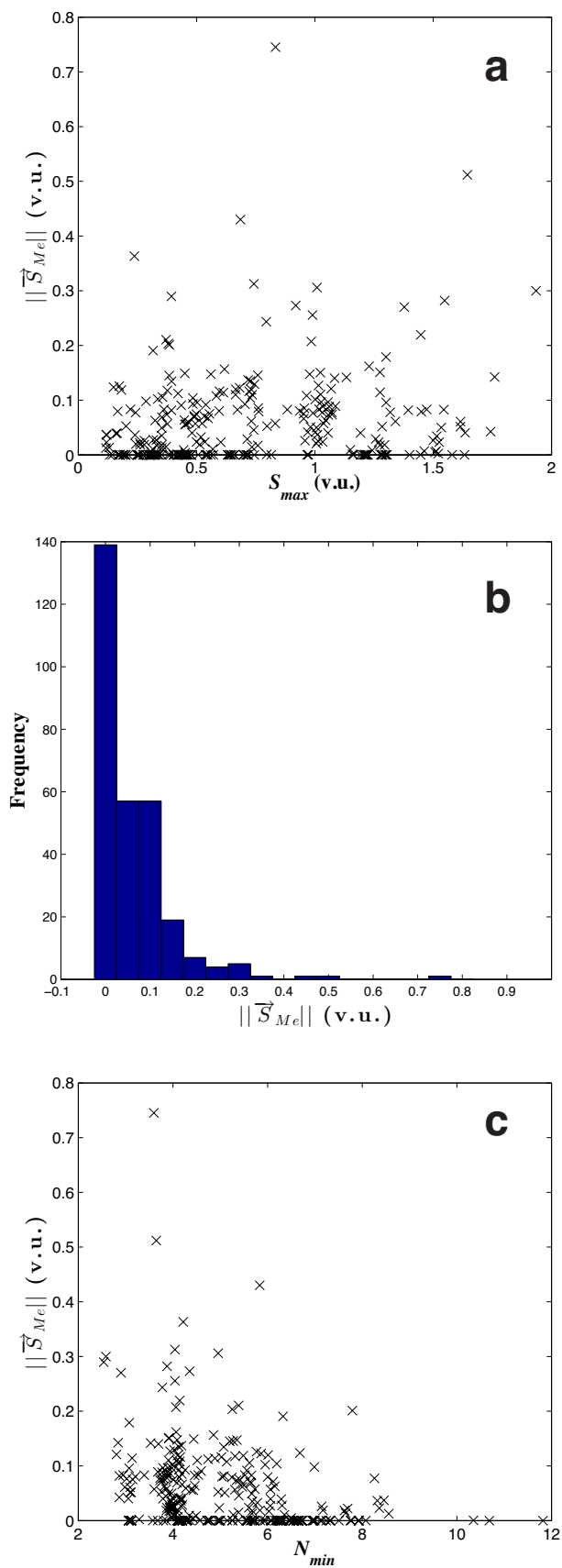
Figure 3

Figure 4

Figure 5

Figure 6